

# High-Pressure, High-Temperature Phase Diagram of Calcium Fluoride from Classical Atomistic Simulations

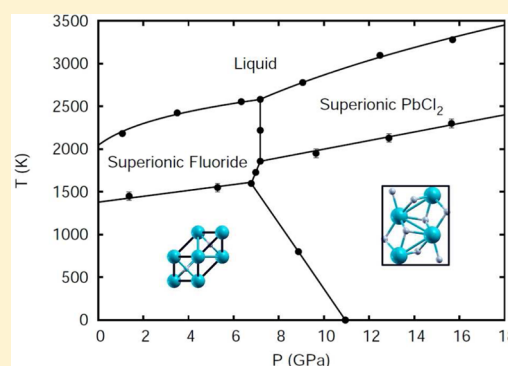
Claudio Cazorla\*

Institut de Ciència de Materials de Barcelona (ICMAB-CSIC), Campus UAB, 08193 Bellaterra, Spain

Daniel Errandonea

Departamento de Física Aplicada (ICMUV), Universitat de Valencia, 46100 Burjassot, Spain

**ABSTRACT:** We study the phase diagram of calcium fluoride ( $\text{CaF}_2$ ) under pressure using classical molecular dynamics simulations performed with a reliable pairwise interatomic potential of the Born–Mayer–Huggins form. Our results obtained under conditions  $0 \leq P \lesssim 20$  GPa and  $0 \leq T \lesssim 4000$  K reveal a rich variety of multiphase boundaries involving different crystal, superionic, and liquid phases, for all of which we provide an accurate parametrization. Interestingly, we predict the existence of three special triple points (i.e., solid–solid–superionic, solid–superionic–superionic, and superionic–superionic–liquid coexisting states) within a narrow and experimentally accessible thermodynamic range of  $6 \leq P \leq 8$  GPa and  $1500 \leq T \leq 2750$  K. In addition, we examine the role of short-ranged repulsive (SR) and long-ranged van der Waals attractive (LA) interactions in the prediction of melting lines with the finding that SR Ca–F and LA F–F contributions are most decisive.



## I. INTRODUCTION

Calcium fluoride ( $\text{CaF}_2$ ) is representative of the fluoride-structured halides, an important family of ionic materials with numerous applications in high-pressure science and technology. Examples of its assorted range of qualities include excellent optical transmission properties over a wide wavelength range, a large electronic band gap, and very high elastic compressibility.<sup>1–5</sup>  $\text{CaF}_2$  is also well-known for being a fast-ion conductor, a material in which the lighter ions (i.e.,  $\text{F}^-$ ) acquire a significant mobility comparable to ionic melts at temperatures well below their fusion point.<sup>6–8</sup> This unusually large diffusion of fluor anions through the almost rigid matrix of calcium cations (i.e.,  $\text{Ca}^{2+}$ ), an effect also termed as superionicity, is originated by the formation of Frenkel pairs and migration of interstitial ions.<sup>7–10</sup> Superionicity, which can also be found in other oxide-, hydride- and iodide-based complexes such as  $\text{Y}_2\text{O}_3$ ,  $\text{LiBH}_4$ , and  $\text{AgI}$ ,<sup>11–14</sup> finds a use in solid state applications as supercapacitors, batteries, and fuel cells.

The intrinsic variety of condensed matter phases in  $\text{CaF}_2$  (i.e., solid, superionic and liquid) a priori suggests a very rich and intriguing  $P$ – $T$  phase diagram. Nevertheless, most of the experimental and theoretical investigations performed so far have focused on very narrow low-pressure and low-temperature thermodynamic ranges. The  $T = 0$  K polymorphism of  $\text{CaF}_2$  encompasses two main crystal structures (see Figure 1): the low-pressure face-centered cubic fluoride phase (space group  $Fm\bar{3}m$ ) and the high-pressure orthorhombic  $\text{PbCl}_2$ -type

(cotunnite) phase (space group  $Pnma$ ). Although  $\text{CaF}_2$  fast-ion conduction has been intensively investigated at ambient pressures,<sup>6–10</sup> it surprisingly remains yet unexplored in the cubic and orthorhombic phases under compression. Gathering information on the pressure dependence of  $\text{CaF}_2$  fast-ion conduction and melting, however, turns out to be very desirable both from a fundamental and technological point of view. Assuming fast-ion conduction behavior in both low- and high-pressure phases, for instance, opens the possibility for the existence of special triple or even quadruple points (i.e., thermodynamic states in which several superionic and solid phases might coexist in thermodynamic equilibrium) at elevated  $P$ – $T$  conditions. Likewise, the expected connections between atomic sublattice melting and homogeneous melting,<sup>15–17</sup> a subject that we have recently investigated in  $\text{Ar}(\text{H}_2)_2$ ,<sup>18,19</sup> are not yet clearly understood. On the practical side, pressure-induced trends unravelled in  $\text{CaF}_2$  could be generalized to other fluoride-structured materials, composed of heavy and light ion species, that have been proposed or are used in relevant technological applications (e.g., transition metal hydrides in hydrogen storage cells and uranium dioxide for generation of nuclear fuel).

In this article, we report the phase diagram of  $\text{CaF}_2$  under pressure (i.e.,  $0 \leq P \lesssim 20$  GPa) as obtained from classical

Received: February 13, 2013

Revised: May 2, 2013

Published: May 3, 2013

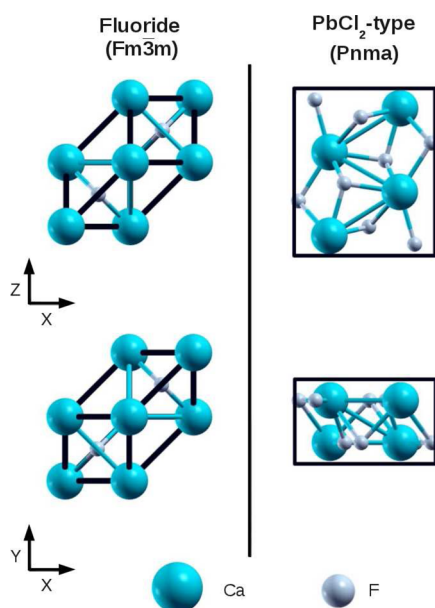


**Figure 1.** Cubic fluoride and orthorhombic  $\text{PbCl}_2$ -type (contunnite) structures of  $\text{CaF}_2$ . In the fluoride structure,  $\text{Ca}^{2+}$  ions are in a cubic close-packed arrangement, and  $\text{F}^-$  ions occupy all the tetrahedral interstitial sites. In the contunnite structure, the array of calcium cations is hexagonal close-packed (hcp), and half the fluor anions are placed off-center in the ideally octahedral hcp voids with 5-fold coordination (the other half of the fluoride ions exhibit tetrahedral coordination). In the fluoride structure, Ca atoms are 8-fold coordinated, whereas in the contunnite structure, the coordination number increases to 9. Calcium and fluor ions are represented with blue and gray spheres, respectively, and the unit cell, with black solid lines.

molecular dynamics (MD) simulations performed with a reliable rigid-ion interatomic potential of the Born–Mayer–Huggins (BMH) form. Our results rely on extensive one- and two-phase coexistence simulations and reveal a rich variety of previously unreported  $P$ – $T$  phase boundaries<sup>15–17</sup> (i.e., fluoride– $\text{PbCl}_2$ , fluoride–liquid,  $\text{PbCl}_2$ –liquid, fluoride–superionic fluoride,  $\text{PbCl}_2$ –superionic  $\text{PbCl}_2$ , superionic fluoride– $\text{PbCl}_2$ , and superionic fluoride–superionic  $\text{PbCl}_2$ ), for all of which we provide here an accurate parametrization. For example, we find that both fluoride–superionic fluoride and  $\text{PbCl}_2$ –superionic  $\text{PbCl}_2$  phase boundaries,  $T_s(P)$ , are linearly dependent on pressure with a small and positive  $dT_s/dP$  slope of 34.2 and 50.2 K/GPa, respectively. Interestingly, we predict the existence of three special triple points involving the coexistence of fluoride–superionic fluoride– $\text{PbCl}_2$ , superionic fluoride– $\text{PbCl}_2$ –superionic  $\text{PbCl}_2$ , and superionic fluoride–superionic  $\text{PbCl}_2$ –liquid phases within a narrow and experimentally accessible region of  $6 \leq P \leq 8$  GPa and  $1500 \leq T \leq 2750$  K. In addition to these findings, we use a free-energy perturbative approach to evaluate the shift in melting temperature caused by mild variations of the employed potential parameters. By doing this, we quantify the role of repulsive and dispersion interactions on our conclusions and qualitatively gain access to the melting features of BMH potentials used in other works.

The organization of this article is as follows: In the section II, we describe the computational methods employed and the low-temperature performance of the selected Born–Mayer–Huggins potential. In section III, we present our results for

the phase diagram of  $\text{CaF}_2$  under pressure and discussions on them. In section IV, we analyze the role of repulsive and dispersion interactions on the determination of melting points by theoretical means. Finally, we summarize the main conclusions in section V.

## II. SIMULATION DETAILS AND THE INTERATOMIC PAIR POTENTIAL

Calculations were performed with LAMMPS,<sup>20</sup> a parallel classical molecular dynamics (MD) code comprising a large variety of potentials and different schemes for simulation of solid-state and soft materials. Our MD calculations are of two main types: one-phase (i.e., pure liquid, solid, and superionic phases) and two-phase coexistence (i.e., liquid and superionic phases coexisting in thermodynamic equilibrium) simulations. One-phase simulations are performed in the canonical ( $N, V, T$ ) ensemble and two-phase coexistence simulations in the microcanonical ( $N, V, E$ ) ensemble (specific details of these simulations are provided in section III). In ( $N, V, T$ ) simulations the temperature is kept fluctuating around a set-point value by using Nose–Hoover thermostats. Large simulation boxes containing 6144 and 12 288 atoms are used in our one-phase and two-phase coexistence simulations, respectively. Periodic boundary conditions are applied along the three Cartesian directions in all the calculations. Newton’s equations of motion are integrated using the customary Verlet’s algorithm and a time-step length of  $10^{-3}$  ps. A particle–particle mesh  $k$ -space solver is used to compute long-range van der Waals and Coulomb interactions and forces beyond a cutoff distance of 12 Å at each time step.

$$V_{ij}(r) = A_{ij}e^{-r/\rho_{ij}} - \frac{C_{ij}}{r^6} + \frac{Z_i Z_j}{r} \quad (1)$$

The interatomic potential adopted for this study is  $U(r) = V_{\text{Ca-F}}(r) + V_{\text{F-F}}(r) + V_{\text{Ca-Ca}}(r)$  where terms  $V_{ij}$  are of the BMH form (see eq 1). Each pairwise term is composed of three different contributions: The first is of exponential type and accounts for the short-ranged atomic repulsion deriving from the overlapping between different electron clouds. The second term is proportional to  $r^{-6}$ , with  $r$  being the radial distance between a given couple of ions, and represents the long-ranged atomic attraction due to dispersive van der Waals forces. The third term is the usual Coulomb interaction between puntual atomic charges, which in our case are taken to be  $Z_{\text{Ca}} = +2e$  and  $Z_{\text{F}} = -1e$ . In Table 1, we enclose the value of the BMH

**Table 1.** Interatomic Pair Potential Parameters for  $\text{CaF}_2$ <sup>a</sup>

	$A$ (eV)	$\rho$ (Å)	$C$ (eV Å) <sup>b</sup>
Ca–F	1717.441	0.287	0.102
F–F	2058.994	0.252	16.703
Ca–Ca	0.0	0.0	0.0

<sup>a</sup>See ref 17. <sup>b</sup>See ref 6.

parameters used throughout this work, which coincide with those recently deduced by Zeng et al.<sup>17</sup> It must be noted that Zeng’s original potential includes electronic polarization effects via a shell model developed by Dick and Overhauser;<sup>21</sup> however, these can be neglected for the present purposes because of the marked ionic nature of  $\text{CaF}_2$ . Indeed, Lindan and Gillan explicitly showed for a similar BMH model that inclusion of electronic polarizability had a remarkably small

effect on the estimation of static and dynamic  $\text{CaF}_2$  quantities.<sup>7,8</sup>

To assess the reliability of the adopted BMH potential, we performed a series of static ground-state calculations and compared them with available low- $T$  experimental data. In Figure 2, we show the zero-temperature equation of state of

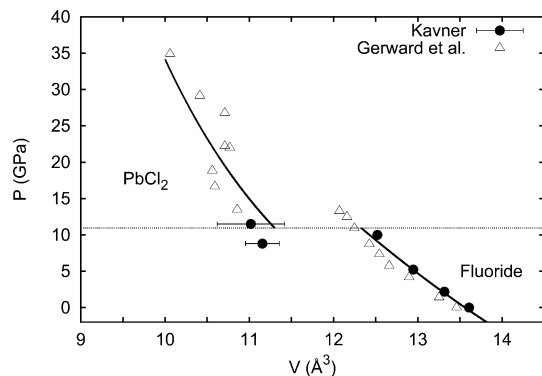


**Figure 2.** Zero-temperature equation of state of  $\text{CaF}_2$  under pressure obtained with the present BMH potential (solid lines). Experimental data can be found in refs 22 and 23.

$\text{CaF}_2$  obtained for its cubic and orthorhombic phases (solid lines). In each phase, we computed the energy per formula unit for a set of 20 volume points spanning over the range  $9.0 \leq V \leq 14.5 \text{ \AA}^3$ . Subsequently, we fitted the results to a third-order Birch–Murnaghan equation of the form

$$E_{\text{perf}}(V) = E_0 + \frac{3}{2} V_0 K_0 x \left[ -\frac{\chi}{2} \left( \frac{V_0}{V} \right)^2 + \frac{3}{4} (1 + 2\chi) \left( \frac{V_0}{V} \right)^{(4/3)} - \frac{3}{2} (1 + \chi) \left( \frac{V_0}{V} \right)^{(2/3)} + \frac{1}{2} \left( \chi + \frac{3}{2} \right) \right] \quad (2)$$

where  $E_0$  and  $K_0 = -V_0(d^2E/dV^2)$  are the energy and bulk modulus at equilibrium volume  $V_0$ , respectively;  $x = 3/4(4 - K'_0)$ ; and  $K'_0 = [\delta K_0/\delta P]$ , with the derivatives taken at zero pressure. (Atomic forces and cell shape relaxations were performed for the orthorhombic  $\text{PbCl}_2$ -type phase at each volume.) The value of the resulting  $E_0$ ,  $V_0$ ,  $K_0$ , and  $K'_0$

parameters are  $-9.05$  ( $-8.97$ ) eV,  $13.56$  ( $12.52$ )  $\text{\AA}^3$ ,  $108.1$  ( $79.5$ ) GPa, and  $1.51$  ( $5.81$ ), respectively, for the cubic (orthorhombic) structure. The static equation of state then is obtained as the minus derivative of eq 2. By comparing the enthalpy of the different phases, we find that the zero-temperature cubic  $\rightarrow$  orthorhombic phase transition occurs at a pressure of  $P_t = 10.9$  ( $0.3$ ) GPa, in very good agreement with recent ambient experimental data  $P_t^{\text{expt}} = 9$  ( $1$ ) GPa obtained by Kavner and others<sup>22,23</sup> (error bars are indicated within the parentheses). The corresponding change of volume is  $-8.35\%$  with  $V = 12.33$  ( $11.30$ )  $\text{\AA}^3$  in the cubic (orthorhombic) phase.

In Table 2, we report the bulk modulus and structural parameters of the two polymorphisms of  $\text{CaF}_2$  obtained at equilibrium and  $P_t$ . As one can see, the agreement with experiment in this case is also notable. It must be noted that from the Birch–Murnaghan fit quoted above, we obtain a zero-pressure bulk modulus that is  $\sim 20$  GPa larger than the experimental value reported by Dorfman et al.<sup>25</sup> However, in the obtaining of that experimental datum, the value of the  $K'_0$  parameter in the corresponding equation of state fit was set to 4.7. Proceeding in the same way as Dorfman and collaborators, we obtain  $K_0 = 82$  ( $5$ ) GPa, which is in very close agreement with their measurements (i.e.,  $K_0^{\text{expt}} = 85$  GPa). Finally, we computed the three independent elastic constants of the  $Fm\bar{3}m$  phase at equilibrium,  $C_{ij}$ 's.<sup>27</sup> We obtain  $C_{11} = 168.1$  ( $0.2$ ),  $C_{12} = 46.9$  ( $0.2$ ), and  $C_{44} = 37.7$  ( $0.2$ ) GPa (error bars are indicated within the parentheses), which agree notably with the experimental values  $C_{11}^{\text{expt}} = 165.4$ ,  $C_{12}^{\text{expt}} = 44.4$  and  $C_{44}^{\text{expt}} = 34.2$  GPa<sup>28</sup> and previous theoretical estimations as well.<sup>17</sup>

The main conclusion emerging from these calculations is that the adopted BMH potential provides a very reliable account of the low- $T$  region of the phase diagram of  $\text{CaF}_2$ . It can then be assumed that medium- and high-temperature descriptions obtained with this same model interaction will be also physically meaningful. In fact, as we will show in the next section, superionic and melting temperatures predicted at ambient pressures are fully consistent with experimental observations.

### III. RESULTS AND DISCUSSION

In the next sections, we describe in detail the two-phase boundaries and special triple points appearing on the phase diagram of  $\text{CaF}_2$  shown in Figure 3; however, let us first explain the general strategy that we followed to obtain it.

**Table 2. Structural Parameters and Bulk Modulus  $K = -V(dP/dV)_T$  of  $\text{CaF}_2$  Obtained at Zero-Temperature<sup>a</sup>.**

	atomic structure ( $\text{\AA}$ )		bulk modulus (GPa)	
	theory	experiment	theory	experiment
$Fm\bar{3}m$ ( $P = 0$ )	$a_0 = 5.460$	$a_0 = 5.463^a$	108 ( $K'_0 = 1.5$ )	
			82 ( $K'_0 = 4.7$ )	$85^b$ ( $K'_0 = 4.7$ )
$Fm\bar{3}m$ ( $P = P_t$ )	$a_0 = 5.289$	$a_0 = 5.313^b$	122	$152$ ( $20$ ) <sup>c</sup>
$Pnma$ ( $P = P_t$ )	$a_0 = 5.721$	$a_0 = 5.700^b$	138	$162$ ( $30$ ) <sup>c</sup>
	$b_0 = 3.463$	$b_0 = 3.450^b$		
	$c_0 = 6.846$	$c_0 = 6.800^b$		
	Ca (0.2472, 0.25, 0.1153)	Ca (0.2530, 0.25, 0.1094) <sup>d</sup>		
	F1 (0.8510, 0.25, 0.0732)	F1 (0.8595, 0.25, 0.0731) <sup>d</sup>		
	F2 (0.4768, 0.25, 0.8300)	F2 (0.4780, 0.25, 0.8344) <sup>d</sup>		

<sup>a</sup>Theory values are obtained with the present BMH potential, and experimental uncertainties are indicated within parentheses.  $P_t = 10.95$  GPa is the pressure at which the cubic  $\rightarrow$  orthorhombic phase transformation is found to occur. Experimental data can be found in refs 24 (a), 25 (b), 23 (c), and 26 (d).

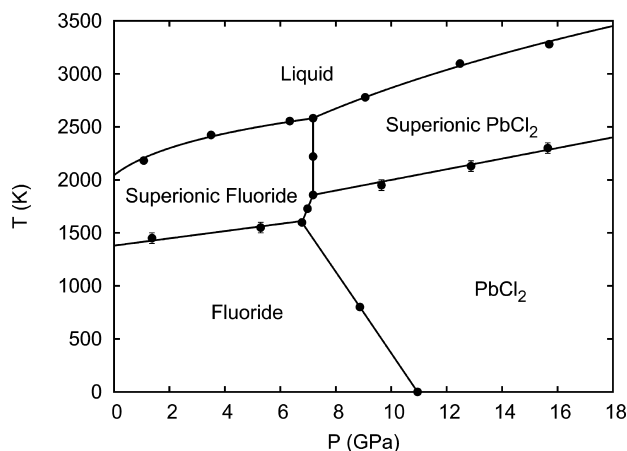


**Figure 3.** The phase diagram of  $\text{CaF}_2$  under pressure obtained from molecular dynamics simulations. Solid lines represent function fits (see text), and solid dots represent thermodynamic states at which molecular dynamic simulations were explicitly carried out. Transition temperature errors are represented with solid bars. Calculated  $(P, T)$  points used in the derivation of the analytical fits (see text) that correspond to thermodynamic metastable states have not been represented in the figure.

Initially, we performed extensive one-phase and two-phase molecular dynamics simulations to find out the solid–superionic and superionic–liquid phase boundaries of the fluoride and  $\text{PbCl}_2$ -type structures in the whole range of pressures considered (i.e.  $0 \leq P \lesssim 20$  GPa). Next, we considered the thermodynamic state  $(P_{1c}, T_{1c})$  at which the melting curves of the two superionic states cross each other. The Gibbs free energy of the superionic fluoride and superionic orthorhombic phases are equal at that thermodynamic state; thus,  $(P_{1c}, T_{1c})$  must belong also to the boundary separating the superionic cubic and superionic orthorhombic regions. In other words,  $(P_{1c}, T_{1c})$  is a special triple point (*special* because it comprises coexistence of superionic and liquid phases, in contrast to ordinary solid–solid–liquid or solid–liquid–vapor triple points). One-phase MD simulations were then carried out to determine the volume and enthalpy (i.e.,  $H = E + PV$ ) of the two superionic phases at  $(P_{1c}, T_{1c})$ . Using the customary Clausius–Clapeyron relation

$$\frac{dT}{dP} = T \frac{\Delta V}{\Delta H} \quad (3)$$

we computed the value of the superionic cubic–superionic orthorhombic boundary slope at that triple point and assumed it to be constant along the multiphase boundary. (In fact, neglecting  $dT/dP$  variations of this type may introduce some errors in our predictions; however, as we will show in section IIIC, these turn out to be rather small.) By tracing the superionic fluoride–superionic  $\text{PbCl}_2$ -type phase boundary, a second special triple point  $(P_{2c}, T_{2c})$  is found at its intersection with the solid orthorhombic–superionic orthorhombic phase boundary (see Figure 3). Likewise, one-phase MD simulations were conducted at  $(P_{2c}, T_{2c})$  to obtain the value of the corresponding  $dT/dP$  slope and assumed it to be constant along the superionic cubic–solid orthorhombic phase boundary. Proceeding as before, we identified the existence of a third special triple point  $(P_{3c}, T_{3c})$  at the crossing of the superionic cubic–solid orthorhombic phase boundary with the solid fluoride–superionic fluoride phase boundary. Finally, the boundary separating the solid cubic and solid orthorhombic

regions was drawn by joining the thermodynamic states  $(P_{3c}, T_{3c})$  and  $(P_v, 0)$ , where  $P_v$  is the pressure at which the cubic  $\rightarrow$  orthorhombic transformation occurs at  $T = 0$ .

In what follows, we describe and yield the parametrization of all the multiphase boundaries cited above, explaining the simulation procedures that we followed to obtain them.

**A. Superionicity.** Comprehensive one-phase  $(N, V, T)$  molecular dynamics simulations were carried out to compute the solid–superionic phase boundary of cubic and orthorhombic  $\text{CaF}_2$  as a function of pressure. Calculations comprised large simulation boxes of 6144 atoms and long simulation times of  $\sim 200$  ps that ensured results free of size-effect bias and achievement of thermodynamic equilibrium (e.g., well-defined energies, equality of the three diagonal components, and nullity of all off-diagonal components of the stress tensor). We systematically carried out simulations at temperature intervals of 100 K up to 3000 K at each volume considered. It must be noted that simulations performed in other thermodynamic ensembles (for instance, the  $(N, P, T)$ ) can also be used for the present purposes, provided that thermodynamic equilibrium conditions are guaranteed.

Following previous works,<sup>7,8,29,30</sup> we identified superionicity via inspection of the time-dependent mean squared displacement function (MSD) obtained in one-phase MD simulations. The MSD function is defined as

$$\langle |\Delta R_i^2(t)| \rangle = \langle |R_i(t + t_0) - R_i(t_0)|^2 \rangle \quad (4)$$

where  $R_i(t)$  is the position of atom  $i$  at time  $t$ ,  $t_0$  is an arbitrary time origin, and  $\langle \dots \rangle$  denotes time average.  $\langle |\Delta R_i^2(t)| \rangle$  was computed separately for each ionic species and time averages were performed over  $t_0$  – that is, every sample point in the simulation was used as a new time origin – and atoms, see Figure 4). In practice,  $\text{F}^-$  diffusion is signaled by the appearance of a nonzero MSD slope, as we illustrate in Figure 4. It is worth noticing that anion diffusion is hardly discernible when scrutinizing only spatially averaged static quantities. For instance, one cannot appreciate important differences between the  $\text{CaF}_2$  radial pair distribution functions obtained at temperatures just above and below the superionic transition (see Figure 5).

For each phase, we determined the superionic transition temperature  $T_s(P)$  at six different volumes. Typical  $T_s$  and  $P_s$  error bars are 50 K and 0.1 GPa, respectively. In both phases, we found that the results could be perfectly fitted to straight lines  $T_s = a_s + b_s P$ , where  $a_s = 1379.69$  K and  $b_s = 34.23$  K/GPa are the optimal parameters for the cubic phase, and  $a_s = 1497.70$  K and  $b_s = 50.17$  K/GPa for the orthorhombic phase (see Figure 3). As can be observed, the slope of both fluoride and  $\text{PbCl}_2$ -type  $T_s(P)$  curves are positive, indicating that the superionic phases are entropically stabilized over the corresponding crystals (i.e., the volume of the former systems is larger than those of the latter  $-0 < \Delta V-$ , and consequently, so is the enthalpy  $-0 < \Delta H-$ ; then  $\Delta H = T\Delta S$  must be accomplished over the coexistence line and  $0 < \Delta S$  follows). This result is reminiscent of customary melting; however, no depletion of the two-phase boundary slope with compression is observed in the present case.

For ambient pressures, we obtain a superionic transition temperature of  $T_s(0) = 1380$  (10) K, which is in very good agreement with experimental data  $T_s^{\text{exp}} = 1420$  (20) K found in refs 31–34. In addition, we computed the diffusion coefficient of  $\text{F}^-$  anions,  $D_-$ , from a least-squares fit to the MSD profiles (i.e.,  $\langle |\Delta R_i^2(t)| \rangle = A_- + 6D_-t$ , following the well-known

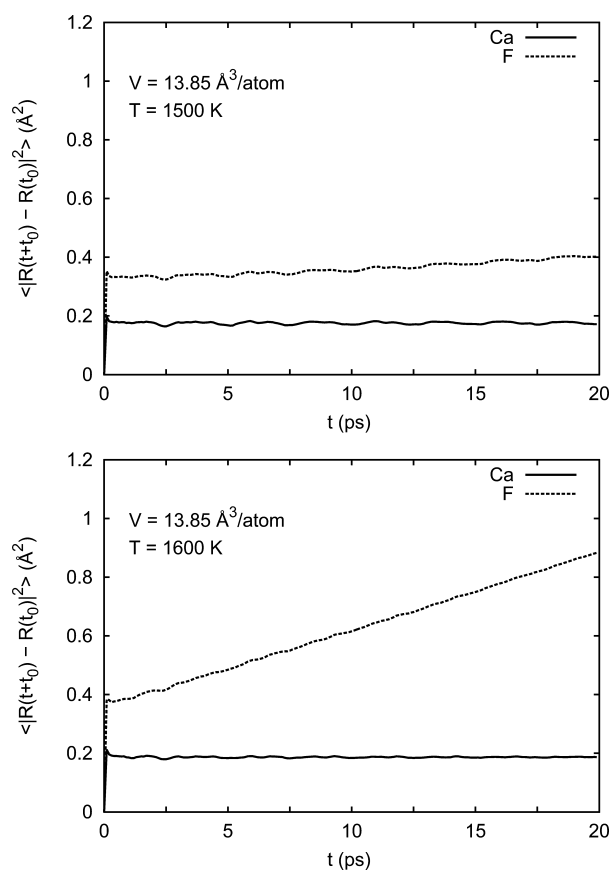


**Figure 4.** Mean squared displacement (MSD) of fluorine and calcium species represented as a function of time at temperatures below (top) and above (bottom) the corresponding transition point  $T_s = 1550$  K. One-phase molecular dynamics simulations were performed for cubic  $\text{CaF}_2$  at pressures of  $\sim 5.3$  GPa. In the top panel, the calculated MSD of the  $\text{F}^-$  anions doubles that of the  $\text{Ca}^+$  cations, signaling the incipient diffusion of the lighter ions.

Einstein relation). Our  $D_-$  results at temperatures 1400, 1500, and 1600 K are 0.3, 0.9, and  $2.7 \times 10^{-5} \text{ cm}^2/\text{s}$ , which turn out to be consistent with experimental data 0.6, 1.6, and  $3.2 \times 10^{-5} \text{ cm}^2/\text{s}$ .<sup>7,9,31,33</sup>

**B. Melting.** Following previous works,<sup>35–40</sup> we performed comprehensive  $(N, V, E)$  two-phase coexistence MD simulations to determine the melting curve of cubic and orthorhombic  $\text{CaF}_2$  under pressure. Starting with a supercell containing the perfect crystal structure (i.e., either fluoride or  $\text{PbCl}_2$ -type), we thermalize it at a temperature slightly below the expected melting temperature for about 10 ps. The system remains in a superionic state. The simulation is then halted, and the positions of the atoms in one-half of the supercell are held fixed while the other half is heated up to a very high temperature (typically 5 times the expected melting temperature) for  $\sim 60$  ps so that it melts completely. With the fixed atoms still fixed, the molten part is rethermalized to the expected melting temperature (for about 10 ps). Finally, the fixed atoms are released, thermal velocities are assigned, and the whole system is allowed to evolve freely at constant  $(N, V, E)$  for a long time (normally more than 100 ps), so that the solid and liquid come into equilibrium (i.e., an equilibrium  $(P, T)$  state is reached; see Figure 6).

The system is monitored by calculating the average number of particles in slices of the cell taken parallel to the boundary

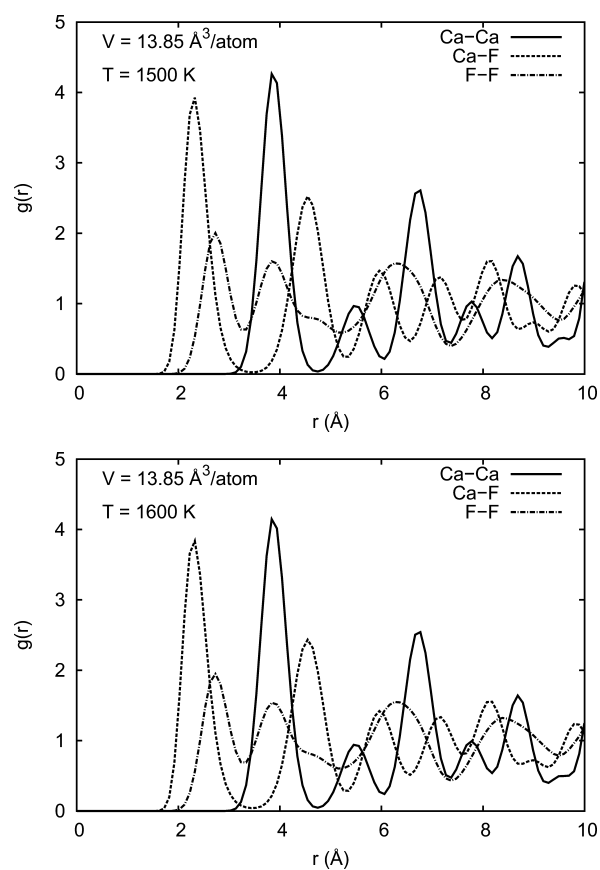


**Figure 5.** Radial pair distribution functions obtained at temperatures below (top) and above (bottom) the corresponding superionic transition point  $T_s = 1550$  K of cubic  $\text{CaF}_2$  at  $P \sim 5.3$  GPa.

between the solid and liquid. With this protocol, there is a certain amount of trial and error to find the overall volume that yields the coexisting solid and liquid system. (An example of a successful coexistence run is shown in Figure 7.) Our simulations were done on cells containing 12 288 atoms with the long axis being perpendicular to the initial liquid–solid boundary. It must be noted that determination of melting states can also be done via simulation of two-phase coexisting systems in the isobaric–isoenthalpic  $(N, P, H)$  ensemble. Despite their differences in implementation, both two-phase coexistence  $(N, V, E)$  and  $(N, P, H)$  approaches must provide equivalent melting results. For a technical description of the  $(N, P, H)$  method, we refer the interested reader to works 42–45. In addition, we note that two-phase  $(N, V, T)$  simulations have been performed to describe liquid and vapor phases in equilibrium.<sup>46,47</sup>

In both cubic and orthorhombic structures, we calculated the melting transition temperature,  $T_m$ , at six different volumes. Typical  $T_m$  and  $P_m$  error bars are 20 K and 0.1 GPa, respectively. We find that our results can be very well fitted to the so-called Simon equation,<sup>48</sup>

$$T_m(P) = a \left( 1 + \frac{P}{b} \right)^c \quad (5)$$

where  $a = 2044.05$  K,  $b = 1.2049$  GPa, and  $c = 0.1202$  are the optimal values for the cubic phase and  $a = 389.19$  K,  $b = 0.0180$  GPa, and  $c = 0.3159$  are for the orthorhombic. Our predicted melting temperature at  $P = 0$  is 2044 (100) K, which turns out to be slightly larger than the experimental value 1690 (20)

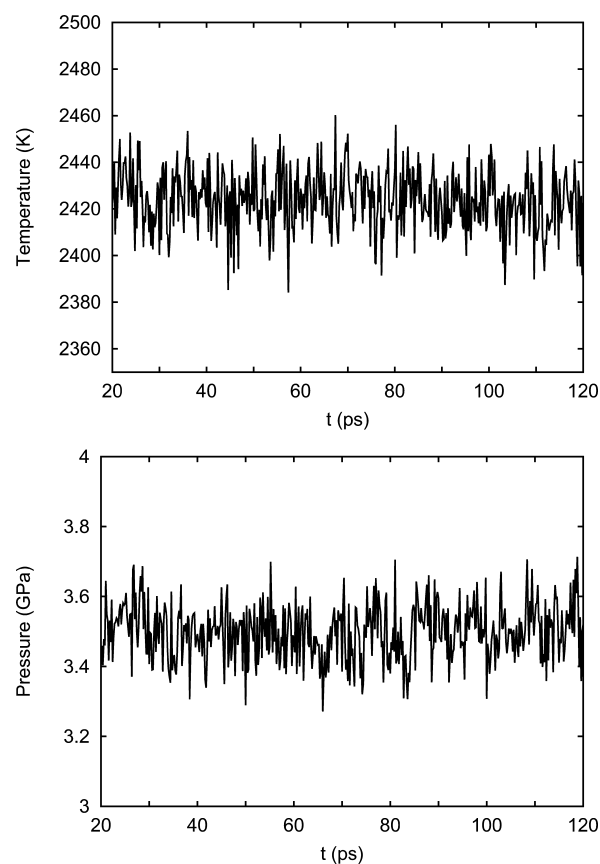


**Figure 6.** Time dependence of the temperature and pressure during a direct simulation of coexisting liquid and solid  $\text{CaF}_2$  using a 12 288-atom supercell.

$\text{K}^{49,50}$  At this temperature, the calculated bulk modulus of the superionic phase is  $\sim 57$  GPa, which is significantly smaller than that obtained for the perfect cubic crystal (see Table 2). Using the Simon equation, we estimate the corresponding zero-pressure melting slope to be  $dT_m/dP = 203.97 \text{ K GPa}^{-1}$ . We note that this quantity is considerably reduced under pressure, in contrast to the constant  $dT_s/dP$  case reported in the previous section. At  $P = 5$  GPa, for instance, we find  $dT_m/dP \sim 40 \text{ K GPa}^{-1}$ . Interestingly, the values of the calculated high- $P$  melting slopes are larger than those measured in alkaline earth (AE) fluorides (e.g., LiF and NaF),<sup>51</sup> despite the structural similarities found between both types of structures. AE fluorides (rock salt) and  $\text{CaF}_2$  (fluorite) both have an fcc array of anions and differ only in the positions of the cations.

A possible cause for the larger melting slope of  $\text{CaF}_2$  could be that AE fluorides melt directly from an ordered crystalline structure, whereas  $\text{CaF}_2$  melts from the superionic phase. Because of diffusion of F atoms, the degree of atomic disorder is larger in superionic  $\text{CaF}_2$  than in rock salt AE fluorides. Therefore, the corresponding entropy of fusion is smaller (and hence,  $\Delta H$ ). Consequently, according to the Clausius–Clapeyron relation, the slope of the melting line should be larger in  $\text{CaF}_2$ . Regarding the melting properties of  $\text{CaF}_2$  in the orthorhombic phase, this exhibits a very low zero-pressure melting point of  $\sim 400$  K (a temperature at which the corresponding crystal structure is metastable) and an overall steep  $dT_m/dP$  slope (see Figure 3). It is worth noticing that the melting line of the orthorhombic phase intersects that of the cubic phase at the special triple point (7.18 GPa, 2580 K). At

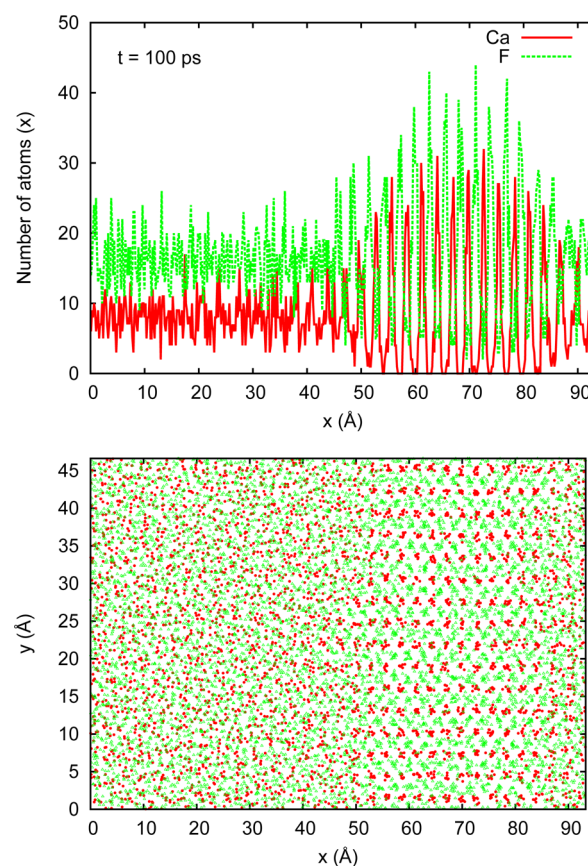


**Figure 7.** Determination of melting temperatures based on two-phase coexistence molecular dynamics simulations. Top: Number of particles histogram represented as a function of position along the direction parallel to the initial solid–liquid boundary. Bottom: Atomic positions projected over the  $x$ – $y$  plane of the simulation box. Calcium and fluorine ions are represented with red and green dots, respectively.

the triple point, an increase occurs in the melting slope. This phenomenon is most likely due to the volume change associated with the solid–solid transition.<sup>52</sup> Unfortunately, we do not know of any experimental data to compare with these results.

Concerning previous  $T_m$  estimations, we are aware only of works done by Zijiang,<sup>15</sup> Wang,<sup>16</sup> and Zeng et al.,<sup>17</sup> who employed pair-potential models similar to those we employed here. The  $P = 0$  melting temperatures predicted by those authors range from 1650 to 2100 K, which are in reasonably good agreement with our results. Nevertheless, we must note that the computational approaches used in those studies consist mainly of one-phase MD simulations and heuristic overheating arguments, both of which are well-known to produce very imprecise  $T_m$  results.<sup>35–39,53,54</sup> In fact, Zeng et al.<sup>17</sup> find a melting temperature of 990–1073 K for the  $Pnma$  phase of  $\text{CaF}_2$  at  $P = 10$  GPa, a result that appreciably differs from our  $T_m = 2867$  K obtained under identical conditions. The main reasons for such discrepancies may probably lie in the different methodologies employed and the complete omission of superionic effects in Zeng’s work.

**C. Special Triple Points and Other Two-Phase Boundaries.** In previous sections, we have characterized four of the seven two-phase boundaries shown in Figure 3. As has been explained at the beginning of this section, we determined the remainder of the boundaries (i.e., solid–solid, solid–

**Table 3. Thermodynamic Data Describing the Unravelling Solid–solid, Solid–superionic, And Superionic–superionic Phase Boundaries<sup>a</sup>**

	$dT/dP$ (K/GPa)	$P_c$ (GPa)	$T_c$ (K)	$\Delta V$ (Å <sup>3</sup> /atom)	$\Delta H$ (eV/atom)
fluoride–PbCl <sub>2</sub>	−315 (40)	6.78 (5)	1600 (10)	−0.97 (2)	0.031 (5)
superionic fluoride–PbCl <sub>2</sub>	650 (100)	7.18 (5)	1860 (10)	−1.01 (2)	−0.023 (5)
superionic fluoride–superionic PbCl <sub>2</sub>	∞	7.18 (5)	2580 (10)	−0.36 (2)	0.00 (5)

<sup>a</sup>The slope of the  $P$ – $T$  boundaries and corresponding changes in volume ( $V$ ) and enthalpy ( $H$ ) at the three special triple points ( $P_c$ ,  $T_c$ ) are reported.

superionic, and superionic–superionic) on the basis of fundamental thermodynamic considerations and one-phase MD simulations and by assuming linear pressure dependence in all of them. The results so obtained are summarized in Table 3. As one can observe, the slope of the superionic fluoride–superionic PbCl<sub>2</sub> boundary is infinite because the calculated enthalpy difference between the two superionic phases at (7.18 GPa, 2580 K) is zero (see Eq. 3). In the other two cases, we find that the slope of the superionic fluoride–PbCl<sub>2</sub> boundary is positive (i.e.,  $\Delta H < 0$  and  $\Delta V < 0$ ) and roughly a factor of 2 larger in absolute value than that of the fluoride–PbCl<sub>2</sub> boundary. In this last case, the resulting  $dT/dP$  slope is negative because the differences in enthalpy and volume between the two crystals are of opposite sign (i.e.,  $\Delta H > 0$  and  $\Delta V < 0$ ). In fact, a priori, one would expect the entropy of the fluoride  $\rightarrow$  PbCl<sub>2</sub> transformation to be positive, and thus,  $\Delta H$ , because higher symmetry structures (i.e., cubic CaF<sub>2</sub>) in general imply lower entropy.

Interestingly, we identify the presence of three special triple points, ( $P_c$ ,  $T_c$ ), in the thermodynamic region  $6 \leq P \leq 8$  GPa and  $1500 \leq T \leq 2750$  K (see Table 3 and Figure 3). These special thermodynamic states are located at the intersections between three different phase boundaries, and the pressures and temperatures at which they are predicted to occur can, in principle, be accessed experimentally. Information contained in Figure 3 and Table 3, hence, must be considered as highly valuable, since identification of coexisting superionic and liquid phases turns out to be very challenging in practice. In fact, we know of just a couple recent experimental works in water wherein coexistence between superionic and liquid phases has been suggested to happen at very extreme  $P$ – $T$  conditions.<sup>55,56</sup>

If one lifted the linear pressure dependence assumption from the solid–solid, solid–superionic, and superionic–superionic phase boundaries, then the location of the three special triple points ( $P_c$ ,  $T_c$ ) quoted in Table 3 will probably change. To quantify the magnitude of those variations, assessing the accuracy in our results, one could, for instance, perform calculations of the Gibbs–Duhem integration type and exactly determine the shape of the involved multiphase boundaries.<sup>57–59</sup> Gibbs–Duhem integration calculations and other equivalent exact schemes,<sup>39,41,53</sup> however, are computationally very intensive, so we opted for a more straightforward test. In particular, we computed the value of the  $dT/dP$  slope at states ( $P_c'$ ,  $T_c'$ ) found at halfway of the approximated linear multiphase boundaries (see Figure 3) and checked whether these differed appreciably from those reported in Table 3. For the superionic cubic–superionic orthorhombic phase boundary, we find that the enthalpy difference between the two phases at (7.18 GPa, 2220 K) is zero, implying also an infinite slope. Assuming linear pressure dependence therefore seems to be adequate in this case. By contrast, at point (6.98 GPa, 1728 K) belonging to the superionic fluoride–solid PbCl<sub>2</sub> boundary, we obtain a  $dT/dP$  value that is roughly 2-fold larger than that obtained at the

corresponding special triple point (7.18 GPa, 1860 K). However, the extent of this last two-phase boundary is so reduced that we may still assume that the resulting ( $P_c$ ,  $T_c$ ) inaccuracies are reasonably small. Certainly, at state (8.87 GPa, 800 K) of the cubic–orthorhombic phase boundary we find  $dT/dP = -300$  (30) K/GPa, which is in very good agreement with the constant assumed value of  $-315$  (40) K/GPa reported in Table 3. These outcomes show that assuming linear pressure dependence in all two-phase boundaries involving superionic and crystal structures provides very consistent results, despite the small errors introduced in the superionic cubic–solid orthorhombic boundary. Consequently, our special triple point estimations can be safely considered as accurate.

#### IV. THE ROLE OF REPULSIVE AND DISPERSION INTERACTIONS ON MELTING

In contrast to *ab initio* electronic band structure methods, empirical and semiempirical force fields may suffer from versatility and transferability issues. This means that an interaction model that correctly describes a set of properties may fail at reproducing others or the same under different thermodynamic constraints. Actually, a considerable number of CaF<sub>2</sub> pairwise potentials are found in the literature, each having been designed for a distinct purpose.<sup>7,9,17,60,61</sup> Trying to derive the phase diagram for all of them would, indeed, be a tedious and extremely boring task. Fortunately, once the phase stability properties of a given interatomic potential are known, it is possible to deduce those for other similar interaction models in a computationally efficient and physically insightful way. We refer here to the original free-energy perturbative approach developed by Gillan and collaborators which has been successfully applied to the study of transition metals under extreme  $P$ – $T$  conditions.<sup>35–37,39,41</sup> In this section, we use Gillan's ideas to compute the shift in melting temperature caused by mild variations of the potential parameters employed through this work (i.e., under the general transformation  $\{X_{ij} \rightarrow X'_{ij}\}$ , where  $\{X_{ij}\}$  corresponds to the set of parameters reported in Table 1). The motivation for this analysis is not only to gain access into the phase diagram features of other similar BMH potentials but also to understand the general role of short- and long-ranged interactions in melting. A brief description of Gillan's free-energy perturbative approach is provided next.

For a given  $P$  and  $T$ , the difference  $G_n^{\text{ls}} \equiv G_n^{\text{l}} - G_n^{\text{s}}$  between the Gibbs free energies of the *new* liquid and solid (i.e., obtained with the *new* set of potential parameters,  $\{X'_{ij}\}$ ) deviates from the corresponding difference  $G_0^{\text{ls}} \equiv G_0^{\text{l}} - G_0^{\text{s}}$  of the initial reference liquid and solid (i.e., obtained with the reference set of potential parameters  $\{X_{ij}\}$  shown in Table 1), and we write

$$G_n^{\text{ls}}(P, T) = G_0^{\text{ls}}(P, T) + \Delta G^{\text{ls}}(P, T) \quad (6)$$

The shift  $\Delta G^{\text{ls}}(P, T)$ , caused by changing the total-energy function from  $U_0$  to  $U_n$ , induces a shift in the corresponding melting temperature  $T_m(P)$ . To first order, the latter shift is<sup>41</sup>

$$\Delta T_m = \frac{\Delta G^{\text{ls}}(T_m^0)}{S_0^{\text{ls}}} \quad (7)$$

where  $S_0^{\text{ls}}$  is the difference between the entropies of the liquid and solid (i.e., the entropy of fusion) of the initial reference system, and  $\Delta G^{\text{ls}}$  is evaluated at the melting temperature of the initial reference system. The shift  $\Delta G^{\text{ls}}$  is the difference of shifts of Gibbs free energies of the liquid and solid caused by the shift  $\Delta U \equiv U_n - U_0$ .<sup>62</sup> Under constant volume and temperature, the shift of the Helmholtz free energy  $\Delta F$  arising from  $\Delta U$  is given by the well-known expansion

$$\Delta F = \langle \Delta U \rangle_0 - \frac{1}{2} \beta \langle \delta \Delta U^2 \rangle_0 + \dots \quad (8)$$

where  $\beta \equiv 1/k_B T$ ,  $\delta \Delta U \equiv \Delta U - \langle \Delta U \rangle_0$ , and the averages are taken in the initial reference ensemble. From  $\Delta F$ , we obtain the shift of Gibbs free energy at constant pressure as

$$\Delta G = \Delta F - \frac{1}{2} V \kappa_T (\Delta P)^2 \quad (9)$$

where  $\kappa_T$  stands for the isothermal compressibility and  $\Delta P$  is the change of pressure caused by the replacement  $U_0 \rightarrow U_n$  at constant  $V$  and  $T$ .

Our  $\Delta T_m$  calculations were performed over series of  $\Delta X_{ij}/X_{ij}$  points ( $\Delta X_{ij} \equiv X'_{ij} - X_{ij}$ , where  $X_{ij}$  refer to the reference potential parameters reported in Table 1) generated in the range  $-25\% \leq \Delta X_{ij}/X_{ij} \leq 25\%$  and taken at 1% intervals (see Figure 8). The averages involved in these calculations were

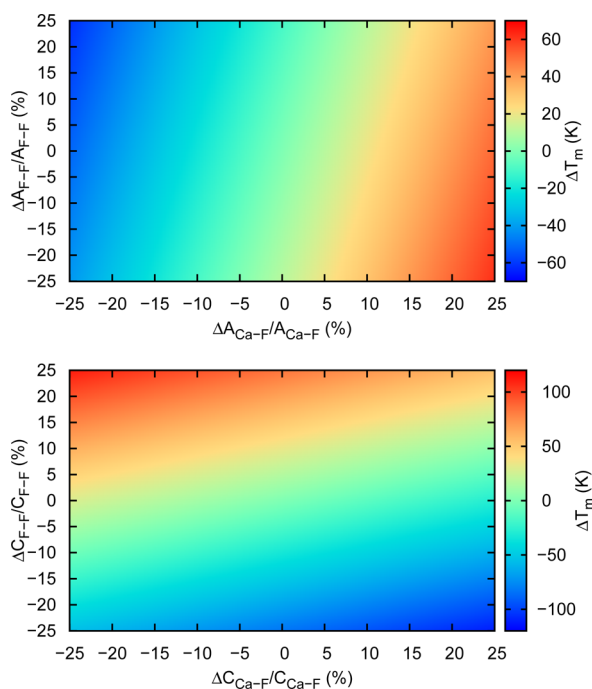


**Figure 8.** Shift of the melting transition temperature  $\Delta T_m$  caused by the variation of potential parameters at  $P_m = 1.0$  GPa and  $T_m = 2180$  K. Top: Short-range repulsive  $A_{\text{Ca-F}}$  and  $A_{\text{F-F}}$  parameters are varied, and the rest of parameters are kept fixed. Bottom: Long-range attractive  $C_{\text{Ca-F}}$  and  $C_{\text{F-F}}$  parameters are varied, and the rest of parameters are kept fixed.

computed over 500 liquid and solid configurations generated in long (i.e.,  $\sim 200$  ps duration) one-phase ( $N, V, T$ ) MD simulations performed with the reference BMH potential (technical details are discussed in section II). These MD simulations were carried out at the arbitrarily selected state (1.0 GPa, 2180 K) lying over the superionic fluoride–liquid phase boundary.

Figure 8 shows our  $\Delta T_m$  results expressed as a function of  $\Delta A_{ij}/A_{ij}$  and  $\Delta C_{ij}/C_{ij}$  variations (i.e., we have neglected  $\rho_{ij}$  fluctuations). As one may appreciate, significant variations of the short-ranged and long-ranged parts of the interatomic potential in general have only a moderate effect on  $T_m$ . For instance,  $A_{ij}$  and  $C_{ij}$  relative variations of  $\sim 25\%$  provoke, at most, melting temperature shifts of  $\sim 100$  K. This result is surprising but at the same time reassuring in the sense that it adds robustness to our  $T_m$  conclusions drawn in the previous section. In particular, if electronic polarizability effects, ignored throughout this work, were to be considered in an effective manner via refitting of the potential parameters, our  $T_m$  results will probably remain unaltered.

Now, let us focus on the  $\Delta T_m$  shifts caused by individual  $A_{\text{FF}}$ ,  $A_{\text{CaF}}$ ,  $C_{\text{FF}}$ , and  $C_{\text{CaF}}$  variations. We note that because of the perturbative character of our approach, the total melting temperature shift provoked by a general  $\{X_{ij} \rightarrow X'_{ij}\}$  transformation is equal to the sum of  $\{\Delta T_m\}$  shifts caused by the individual  $X_{ij}$  fluctuations. Concerning the short-ranged part of the interaction model (see top of Figure 8), we find that reduction of the  $A_{\text{FF}}$  parameter causes a positive melting temperature shift; by contrast, an increase in the same parameter leads to  $\Delta T_m < 0$ . This outcome shows that strengthening (weakening) of the repulsive F–F interactions tends to further stabilize (destabilize) the liquid phase. Interestingly, we observe the opposite trend for  $A_{\text{CaF}}$ :  $\Delta A_{\text{CaF}} < 0$  fluctuations lead to  $\Delta T_m < 0$  (i.e., the liquid phase is energetically favored), whereas  $\Delta A_{\text{CaF}} > 0$  leads to  $\Delta T_m > 0$  (i.e., the liquid phase is energetically disfavored). Upon a similar  $\Delta A_{ij}/A_{ij}$  change, we observe that the melting temperature shift obtained in the  $A_{\text{FF}}$  case is the smallest (in absolute value) (e.g.,  $\Delta T_m = -10$  and 51 K for  $\Delta A_{\text{FF}}/A_{\text{FF}}$  and  $\Delta A_{\text{CaF}}/A_{\text{CaF}} = 25\%$ , respectively); thus, repulsive Ca–F interactions play a more dominant role in melting.

Regarding the long-ranged attractive part of the interaction model (see bottom of Figure 8), the situation is the opposite of that just explained. In particular,  $\Delta C_{\text{FF}} < 0$  ( $\Delta C_{\text{FF}} > 0$ ) changes lead to  $\Delta T_m < 0$  ( $\Delta T_m > 0$ ), and  $\Delta C_{\text{CaF}} < 0$  ( $\Delta C_{\text{CaF}} > 0$ ) leads to  $\Delta T_m > 0$  ( $\Delta T_m < 0$ ). Moreover, upon the same  $\Delta C_{ij}/C_{ij}$  variation, the melting temperature shift obtained in the  $C_{\text{FF}}$  case is the largest (in absolute value) (e.g.,  $\Delta T_m = 83$  and  $-29$  K for  $\Delta C_{\text{FF}}/C_{\text{FF}}$  and  $\Delta C_{\text{CaF}}/C_{\text{CaF}} = 25\%$ , respectively); thus, attractive F–F interactions play a more important role in melting. As a summary of these results, we can state that short-ranged repulsive Ca–F and long-ranged attractive F–F contributions to melting are the most important and that reduction (increase) of the involved parameters  $A_{\text{CaF}}$  and  $C_{\text{FF}}$  leads to further stabilization (destabilization) of the liquid over the cubic superionic phase.

Finally, we can use our results shown in Figure 8 to predict, at least at a qualitative level, the melting features corresponding to other developed  $\text{CaF}_2$  BMH potentials. In particular, we examine two parametrizations proposed by Gillan<sup>7</sup> and Boufelfel.<sup>60</sup> For the sake of simplicity, we consider here only  $\Delta T_m$  contributions stemming from the dominant  $A_{\text{CaF}}$  and  $C_{\text{FF}}$  parameters. For Gillan's parametrization, we obtain  $\Delta A_{\text{CaF}}/$

$\Delta A_{\text{CaF}} \sim -60\%$  and  $\Delta C_{\text{FF}}/C_{\text{FF}} \sim 550\%$ . Actually, these values turn out to be exceedingly large so as to being treated within our perturbative approach; however, we can make a qualitative statement on the basis of the size and sign of those deviations. In particular, the  $C_{\text{FF}}$  difference is eminently the largest and positive so that the resulting temperature correction is very likely to be positive and large (i.e.,  $T_m \gg 2180$  K). In the case of Boulfelfel's potential, we obtain  $\Delta A_{\text{CaF}}/\Delta A_{\text{CaF}} \sim -72\%$  and  $\Delta A_{\text{CaF}}/\Delta A_{\text{CaF}} \sim -100\%$ . These values are of opposite sign to Gillan's and still too large to be analyzed using our method. Nevertheless, at the qualitative level, we can state that the resulting  $\Delta T_m$  difference is very likely to be negative and small since the  $C_{\text{FF}}$  deviation is negative and only slightly superior to  $A_{\text{CaF}}$  (i.e.,  $T_m \lesssim 2180$  K).

As a concluding remark to this section, we mention that the computational strategy just presented can also be applied to the analysis of multiphase boundaries other than melting and, in general, to modeling of atomic interactions for derivation of phase diagrams.

## V. CONCLUSIONS

To summarize, we have studied the phase diagram of  $\text{CaF}_2$  under pressure using classical atomistic simulations and a pairwise interatomic potential of the Born–Mayer–Huggins form. Our results show that a rich variety of crystal, superionic, and liquid phases coexist within the thermodynamic region  $0 \leq P \lesssim 20$  GPa and  $0 \leq T \lesssim 4000$  K. In particular, we find seven different two-phase boundaries for all of which we provide an accurate parametrization. Interestingly, three special triple points are predicted to exist within the narrow and experimentally accessible thermodynamic range of  $6 \leq P \leq 8$  GPa and  $1500 \leq T \leq 2750$  K. Indeed, we believe that these stimulating findings should encourage new experimental searches in  $\text{CaF}_2$  under elevated  $P$ – $T$  conditions. In addition, we have analyzed the role of short-ranged repulsive and long-ranged van der Waals attractive interactions in the prediction of melting points, with the finding that repulsive Ca–F and attractive F–F contributions are the most important. To get rid of possible versatility and transferability force-field issues, such as in the modeling of electronic polarizability effects, it would be very much desirable to conduct ab initio simulation studies similar to the one presented here. Work in this direction is already in progress within our group.

## ■ AUTHOR INFORMATION

### Notes

The authors declare no competing financial interest.

## ■ ACKNOWLEDGMENTS

This work was supported by MICINN-Spain (Grants No. MAT2010-18113, CSD2007-00041, MAT2010-21270-C04-01, CSD2007-00045, and FIS2008-03845), and computing time was kindly provided by CESGA.

## ■ REFERENCES

- (1) Barth, J.; Johnson, R. L.; Cardona, M.; Fuchs, D.; Bradshaw, A. M. *Phys. Rev. B* **1990**, *41*, 3291.
- (2) Gan, F.; Xu, Y. N.; Huang, Z. M.; Ching, Y. W.; Harrison, G. J. *Phys. Rev. B* **1992**, *45*, 8248.
- (3) Verstraete, M.; Gonze, X. *Phys. Rev. B* **2003**, *68*, 195123.
- (4) Shi, H.; Eglitis, I. R.; Borstel, G. *Phys. Rev. B* **2005**, *72*, 045109.
- (5) Sata, N.; Shen, G. Y.; Rivers, M. L.; Sutton, S. R. *Phys. Rev. B* **2002**, *65*, 104114.

- (6) Hayes, W.; Stoneham, A. M. In *Defects and Defect Processes in Non-metallic Solids*; Wiley: New York, 1985.
- (7) Gillan, M. J. *J. Phys. C* **1986**, *19*, 3391; *J. Chem. Soc. Faraday Trans.* **1990**, *86*, 1177.
- (8) Lindan, P. J. D.; Gillan, M. J. *J. Phys.: Condens. Matter* **1993**, *5*, 1019.
- (9) Wilson, N. T.; Wilson, M.; Madden, P. A.; Pyper, N. C. *J. Chem. Phys.* **1996**, *105*, 11209.
- (10) Montani, R. A. *J. Chem. Phys.* **1994**, *100*, 8381.
- (11) Lehovec, K. *J. Chem. Phys.* **1953**, *21*, 1123.
- (12) Matsuo, M.; Nakamori, Y.; Orimo, S.-I.; Maekawa, H.; Takamura, H. *Appl. Phys. Lett.* **2007**, *91*, 224103.
- (13) Shevlin, S. A.; Cazorla, C.; Guo, Z. X. *J. Phys. Chem. C* **2012**, *116*, 13488.
- (14) Stuhmann, C. H. J.; Kreiterling, H.; Funke, K. *Solid State Ionics* **2002**, *154*, 109.
- (15) Zijiang, L.; Xiangrong, C.; Jianhong, Q.; Huazhong, G. *Chin. J. Chem. Phys.* **2005**, *18*, 193.
- (16) Wang, C.-S. *Bull. Mater. Sci.* **2010**, *33*, 413.
- (17) Zeng, Z.-Y.; Chen, X.-R.; Zhu, J.; Hu, C.-E. *Chin. Phys. Lett.* **2008**, *25*, 230.
- (18) Cazorla, C.; Errandonea, D. *Phys. Rev. B* **2010**, *81*, 104108.
- (19) Cazorla, C.; Errandonea, D.; Sola, E. *Phys. Rev. B* **2009**, *80*, 064105.
- (20) Plimpton, S. J.; Comp., J. *Phys.* **1995**, *117*, 1 <http://lammps.sandia.gov>.
- (21) Dick, B. G.; Overhauser, A. W. *Phys. Rev.* **1958**, *112*, 90.
- (22) Kavner, A. *Phys. Rev. B* **2008**, *77*, 224102.
- (23) Gerward, L.; Olsen, J. S.; Steenstrup, S.; Malinowski, M.; Asbrink, S.; Waskowska, A. *J. Appl. Crystallogr.* **1992**, *25*, 578.
- (24) Wu, X.; Wu, Z. Y.; Guo, L.; Liu, C.; Liu, J.; Li, X. D. *Solid State Commun.* **2005**, *135*, 780.
- (25) Dorfman, S. M.; Jiang, F.; Mao, Z.; Kubo, A.; Meng, Y.; Prakapenka, V. B.; Duffy, T. S. *Phys. Rev. B* **2010**, *81*, 174121.
- (26) Morris, E.; Groy, T.; Leinenweber, K. *J. Phys. Chem. Solids* **2001**, *62*, 1117.
- (27) Shi, H.; Luo, W.; Johansson, B.; Ahuja, R. *J. Phys.: Condens. Matter* **2009**, *21*, 415501.
- (28) Catti, M.; Dovesi, R.; Pavese, A.; Saunders, V. R. *J. Phys.: Condens. Matter* **1991**, *3*, 4151.
- (29) Yin, W.-G.; Liu, J.; Duan, C.-G.; Mei, W. N.; Smith, R. W.; Hardy, J. R. *Phys. Rev. B* **2004**, *70*, 064302.
- (30) Araújo, C. M.; Blomqvist, A.; Scheicher, R. H.; Chen, P.; Ahuja, R. *Phys. Rev. B* **2009**, *79*, 172101.
- (31) Derrington, C. E.; Lindner, A.; O'Keeffe, M. *J. Solid State Phys.* **1975**, *15*, 171.
- (32) Hayes, W.; and Hutchings, M. T.; in *Ionic Solids at High Temperatures*, (World Scientific, Singapore 1985).
- (33) Evangelakis, G. A.; Pontikis, V. *Europhys. Lett.* **1989**, *8*, 599.
- (34) Dixon, M.; Gillan, M. J. *J. Phys. (Paris)* **1980**, *41*, C6–24.
- (35) Cazorla, C.; Gillan, M. J.; Taioli, S.; Alfè, D. *J. Chem. Phys.* **2007**, *126*, 194502.
- (36) Taioli, S.; Cazorla, C.; Gillan, M. J.; Alfè, D. *Phys. Rev. B* **2007**, *75*, 214103.
- (37) Cazorla, C.; Alfè, D.; Gillan, M. J. *J. Chem. Phys.* **2009**, *130*, 174707.
- (38) Alfè, D.; Cazorla, C.; Gillan, M. J. *J. Chem. Phys.* **2011**, *135*, 024102.
- (39) Cazorla, C.; Alfè, D.; Gillan, M. J. *Phys. Rev. B* **2012**, *85*, 064113.
- (40) Alfè, D. *Phys. Rev. B* **2009**, *79*, 060101(R).
- (41) Alfè, D.; Gillan, M. J.; Price, G. D. *J. Chem. Phys.* **2002**, *116*, 6170.
- (42) Wang, J.; Yoo, S.; Bai, J.; Morris, J. R.; Zeng, X. C. *J. Chem. Phys.* **2005**, *123*, 036101.
- (43) Yoo, S.; Zeng, X. C.; Morris, J. R. *J. Chem. Phys.* **2004**, *120*, 1654.
- (44) Hernández, E. R. *J. Chem. Phys.* **2001**, *115*, 10282.
- (45) Wang, L. G.; van de Walle, A.; Alfè, D. *Phys. Rev. B* **2011**, *84*, 092102.

- (46) Alexandre, J.; Tildesley, D. J.; Chapela, G. A. *J. Chem. Phys.* **1995**, *102*, 4574.
- (47) Liew, C. C.; Inomata, H.; Arai, K. *Fluid Phase Equilib.* **1998**, *144*, 287.
- (48) Simon, F. E.; Glatzel, G.; Anorg. *Z. u. Allgem. Chem.* **1929**, *178*, 309.
- (49) McLaughlan, S. D. *Phys. Rev.* **1967**, *160*, 287.
- (50) Mitchell, A.; Joshi, S. *Metall. Trans.* **1972**, *3*, 2306.
- (51) Boehler, R.; Ross, M.; Boercker, D. B. *Phys. Rev. Lett.* **1997**, *78*, 4589.
- (52) Errandonea, D.; Boehler, R.; Ross, M. *Phys. Rev. B* **2002**, *65*, 012108.
- (53) Haskins, J. B.; Moriarty, J. A.; Hood, R. Q. *Phys. Rev. B* **2012**, *86*, 224104.
- (54) Hernández, E. R.; Rodríguez-Prieto, A.; Bergara, A.; Alfé, D. *Phys. Rev. Lett.* **2010**, *104*, 185701.
- (55) Goncharov, A. F.; Sanloup, C.; Goldman, N.; Crowhurst, J. C.; Bastea, S.; Howard, W. M.; Fried, L. E.; Guignot, N.; Mezouar, M.; Meng, Y. *J. Chem. Phys.* **2009**, *130*, 124514.
- (56) Sugimura, E.; Komabayashi, T.; Ohta, K.; Hirose, K.; Ohishi, Y.; Dubrovinsky, L. S. *J. Chem. Phys.* **2012**, *137*, 194505.
- (57) Kofke, D. A. *J. Chem. Phys.* **1993**, *98*, 4149.
- (58) Sanz, E.; Vega, C.; Abascal, J. L. F.; MacDowell, L. G. *Phys. Rev. Lett.* **2004**, *92*, 255701.
- (59) McBride, C.; Noya, E. G.; Aragoes, J. L.; Conde, M. M.; Vega, C. *Phys. Chem. Chem. Phys.* **2012**, *14*, 10140.
- (60) Boulfelfel, S. E.; Zahn, D.; Hochrein, O.; Grin, Y.; Leoni, S. *Phys. Rev. B* **2006**, *74*, 094106.
- (61) Speziale, S.; Duffy, T. S. *Phys. Chem. Miner.* **2002**, *29*, 465.
- (62) Zwanzig, R. W. *J. Chem. Phys.* **1954**, *22*, 1420.